Supplement of Geosci. Model Dev., 14, 5999–6023, 2021
https://doi.org/10.5194/gmd-14-5999-2021-supplement

Geoscientific
Model Development

Supplement of

A model for marine sedimentary carbonate diagenesis and paleoclimate proxy signal tracking: IMP v1.0

Yoshiki Kanzaki et al.

Correspondence to: Yoshiki Kanzaki (ykanzaki3@gatech.edu)

S1. Model options

S1.1. Signal tracking method

S1.1.1. Time-stepping method

IMP can adopt the time-stepping method (method 1 in Fig. 3a) as an option. In this section, the time-stepping method is used for dissolution experiment #2 of Section 3.2.2 and results are compared with those by method 2. The isotope signal changes in δ^{13}C and δ^{18}O are discretized into 42 steps, represented by 42 classes of $CaCO_3$ particles with distinct signals (Fig. S1) as described in Section 2.4.1.

When using the time-stepping method with 42 different $CaCO_3$ classes for dissolution experiment #2, very similar results are obtained to those with the interpolating method (compare Figs. S2a–c and S2d–f). Results of the time-stepping method approach the interpolation method results when the total number of $CaCO_3$ classes is increased. Furthermore, other simulations adopting the time-stepping method lead to the same degree of agreement of the results (e.g., dissolution experiment #1). Such comparisons confirm that signal tracking diagenesis can be simulated by either method 1 or 2 but a large number of $CaCO_3$ classes is required when adopting method 1.

S1.1.2. Direct tracking of $CaCO_3$ isotopologues

As another option, IMP is able to directly track temporal changes of spatial distributions of five $CaCO_3$ isotopologues: $Ca^{12}C^{16}O_3$, $Ca^{12}C^{18}O^{16}O_2$, $Ca^{13}C^{16}O_3$, $Ca^{13}C^{18}O^{16}O_2$ and $Ca^{14}CO_3$. This option is a specific application of the direct tracking method (method 3 in Fig. 3c) and is beneficial because it allows tracking of ^{14}C age and Δ_{47}, in addition to δ^{13}C and δ^{18}O, in a computationally efficient way (Section 2.4.1). For ^{14}C age tracking the radioactive decay of $Ca^{14}CO_3$ and accompanying generation of alkalinity (through assumed production of nitrate ^{14}N) are accounted for:

$$R_\ell = (1-\phi) m_\ell k_{\mathrm{cc},\ell} (1-\varOmega_{\mathrm{cc}})^{\eta_{\mathrm{cc}}} H(1-\varOmega_{\mathrm{cc}}) + (1-\phi) m_\ell \lambda_\ell \tag{S1}$$

$$R_{\mathrm{ALK}} = (1-\phi) m_{\mathrm{OM}} k_{\mathrm{anox}} + \sum_{\ell=1}^{n_{\mathrm{cc}}} 2(1-\phi) m_\ell k_{\mathrm{cc},\ell} (1-\varOmega_{\mathrm{cc}})^{\eta_{\mathrm{cc}}} H(1-\varOmega_{\mathrm{cc}}) + (1-\phi) m_\ell \lambda_\ell \tag{S2}$$

where ℓ is one of n_{cc} $CaCO_3$ classes including $Ca^{14}CO_3$ and $Ca^{12}CO_3$, and λ_ℓ is the decay constant which is 8033^{-1} yr^{-1} for $Ca^{14}CO_3$ (Aloisi et al., 2004) and zero for all other classes. With method 3, Eqs. (S1) and (S2) can be implemented instead of Eqs. (5) and (9) for ^{14}C age tracking. Apart from the implementation of Eqs. (S1) and (S2) instead of Eqs. (5) and (9) the model calculation and application to signal tracking are the same as described in Section 2.

As an example for the direct tracking of $CaCO_3$ isotopologues, we conduct again dissolution experiment #2 as presented in Section 3.2.2. Here changes in Δ_{47} in $CaCO_3$ are imposed additionally and are assumed synchronous with the δ^{18}O changes (Fig. S3). The rain fluxes of individual isotopologues (Fig. S3b) are calculated directly from the input signals (Fig. S3a), except for the $Ca^{14}CO_3$ flux, which is calculated assuming that the $^{14}C/^{12}C$ ratio is constant at 1.2×10^{-12} (Aloisi et al., 2004). Note that the changes in rain fluxes with time are hard to discern from the semi-log plot of Fig. S3b. Another set of the five isotopologues needs to be additionally simulated when one further tracks model time as a proxy.

Obtained signals of $\delta^{13}C$ and $\delta^{18}O$ as well as $CaCO_3$ abundance (Fig. S4a–c) are the same as those obtained by method 2 (Figs. 13g–i), thus validating the direct tracking method. As the imposed temporal changes for Δ_{47} are the same as those for $\delta^{18}O$ (Fig. S3a), the same patterns of signal distortion are obtained for both signals (Figs. S4b and e). The ^{14}C age is increased from ∼5 up to ∼50 kyr by dissolution (Fig. S4d), which is consistent with previous results (e.g., Keir, 1984; Broecker et al., 1991; Oxburgh, 1998; Barker et al., 2007), but with our model, we can further examine the effects of different styles of bioturbation as well as different extents of dissolution (e.g., Fig. S4d). Note, however, that ^{14}C ages plotted against diagnosed depth do not reflect ^{14}C decay below the mixed layer (Section 2.4.2 and Fig. 5).

As an interesting feature of the option, we can further examine the kinetic isotope effect on signal distortion. As an example, assuming −0.005% of kinetic isotope effect for dissolution of $Ca^{13}C^{18}O^{16}O_2$ (i.e., $k_{\mathrm{cc,Ca^{13}C^{18}O^{16}O_2}} = (1 - 5 \times 10^{-5}) \times 365.25\ \mathrm{yr}^{-1}$), quite large signal distortions on Δ_{47} are predicted (dotted curves in Fig. S4f). Although the kinetic isotope effect for $CaCO_3$ dissolution is not known due to the lack of experimental report (DePaolo, 2011), we can examine a hypothetical kinetic isotope effect for any isotopologues (not limited to $Ca^{13}C^{18}O^{16}O_2$) on signal distortion by changing $k_{\mathrm{cc},\ell}$ values. For example, simulations with various extents of dissolution (e.g., dissolution experiment #1 of Section 3.2.2) and $k_{\mathrm{cc},\ell}$ values suggest that signal distortion can be dominated by the kinetic isotope effect when the kinetic isotope effect is relatively large and/or dissolution is intense.

S1.2. Implicit implementation of an OM-degradation-associated reaction

OM degradation explicitly simulated in the current version of IMP is limited to oxidation by O_2 and SO_4. Other OM reaction pathways are thus ignored, which is not an unreasonable simplification given their relatively minor importance on the global scale (Section 2.2.1). However, one can still add a set of artificial DIC and ALK fluxes at a given depth to implicitly simulate an OM-related reaction and (at least partly) fill the lack of a detailed OM reaction network as a user option though currently only usable in the Fortran version.

To illustrate the utility of this model option, here we conduct a set of diagenetic experiments. In the first, steady-state bulk profiles are obtained in the same way as we obtained the profiles in Fig. 6, except now the water depth is 4 km and the total sediment depth (z_{tot}) is 200 m (‘CTRL’ in Fig. S5). In the second run, we add 12 and 24 $\mu\mathrm{mol\ cm^{-2}\ yr^{-1}}$ of DIC and ALK fluxes, respectively, at 10 m sediment depth, from assumed deep occurence of anoxic oxidation of methane (AOM) (‘+AOM at 10 m’ in Fig. S5). The two fluxes are added assuming normal distributions centered at 10 m with 1 m standard deviation. We also allow precipitation of $CaCO_3$ by removing the Heaviside function from Eq. (5) for both experments.

Because of the addition of DIC and ALK fluxes from AOM, porewater gets supersaturated with respect to $CaCO_3$ at depth, and resultant authegenic $CaCO_3$ adds ~20 wt% to the background $CaCO_3$ in the control run where AOM is not imposed. The two experiments demonstrate the utility of the option to examine the effect of a specific OM-related reaction on $CaCO_3$ diagenesis, aided also by the flexibility of the grid structure in IMP (compare Figs. S5 and 6; see also Section S1.4).

S1.3. Utilization of CO_2 chemistry calculation modules

IMP has the option to adopt improved routines to model the ocean carbonate system, i.e., mocsy 2.0 (Orr and Epitalon, 2015, for the Fortran and Python versions) and CO2SYS (Lewis and Wallace, 1998; van Heuven et al., 1998; Humphreys et al., 2020, for the Python and MATLAB versions), as a replacement for the simplified calculation summarized in Tables 2 and 3. With the more complicated and realistic calculations of CO_2 chemistry by mocsy 2.0 and CO2SYS, diagenetic results are modified, but responses of $CaCO_3$ to undersaturation are not so significantly affected (Figs. S6 and S7, compare with Figs. 8 and 9). Nonetheless, the option is beneficial because changes in CO_2 chemistry caused by a comprehensive set of environmental factors (including aqueous species other than carbonate species) can be explicitly reflected in $CaCO_3$ diagenesis and proxy signals.

S1.4. Grid structure of model sediment

The grid structure of modeled sediment is determined by the total sediment depth (z_{tot}) and a parameter β that determines how the sediment layer thickness changes with sediment depth: the grid becomes more irregular as β approaches 1 (Table 2; cf. Hoffman and Chiang, 2000). The default grid structure adopted in the main text is a relatively deep and highly irregular sediment grid where $z_{\mathrm{tot}} = 500$ cm and $\beta = 1 + 5 \times 10^{-11}$. As a beneficial feature of IMP, one can adopt a different grid structure that suits the user's interest (cf. Section S1.2), although the changes in the above two parameters have to be made within the codes.

As an example of such a user option, we repeat the dissolution experiments in Section 3.2.2 but now adopting a shallower ($z_{\mathrm{tot}} = 50$ cm) and less irregular ($\beta = 1.05$) sediment grid. Despite significant difference in the grid structure, temporal changes of depth profiles are similar to those with the grid adopted in the main text (compare e.g., Figs. S8 and 7). Signal tracking methods in Section 2.4.2 can also be found efficient to minimize the effects of numerical diffusion on tracked signals regardless of the grid structure because very similar proxy signals are simulated from the two grids (compare Figs. S9 and 13).

S1.5. Time tracking

We illustrated signal tracking diagenesis with the interpolating method (method 2, Section 2.4.1) in Section 3.2. Simulations in Sections 3.2.1 and 3.2.2 track 2 paleoceanographic proxies δ^{13}C and δ^{18}O with 4 classes of $CaCO_3$ particles that have the maximum and/or minimum values of input δ^{13}C and δ^{18}O. In Section 3.2.3, we doubled the number of $CaCO_3$ classes (i.e., adopted 8 classes) to track the δ^{13}C and δ^{18}O in two distinctive model species ('fine' vs. 'coarse' species). By adopting 8 classes of $CaCO_3$ particles that have the endmember values of δ^{13}C and δ^{18}O and size-dependent dissolution and mixing properties, one can track not only δ^{13}C and δ^{18}O, but also the size distribution in bulk $CaCO_3$ in simulations in Section 3.2.3 (cf. Fig. 15c). Thus, a simple relationship can apply to method 2: when one tracks n_p proxies and/or characteristics (e.g., size) of bulk $CaCO_3$, 2^{n_p} classes of $CaCO_3$ particles are necessary as described in Section 2.4.1.

Trackable characteristics with method 2 include model time (Section 2.4.2). As an example, consider a simplest case where one tracks only the average model time in bulk $CaCO_3$ but not any other proxies or characteristics. This case requires two classes of $CaCO_3$ particles with the minimum (or start) and maximum (or final) model-time. The model time can be tracked by assigning rain fluxes to the two classes of $CaCO_3$ particles so that flux-weighted average mode-time of the two classes matches the model time of the simulation. For example, the total carbonate rain flux is dominated by the $CaCO_3$ class with the minimum model-time at the start of the simulation, equally contributed by the two classes at the middle of the simulation and is dominated by the class with the maximum model-time at the end of simulation. More generally, one can additionally track model time by doubling the number of $CaCO_3$ classes that are used for simulations without time tracking.

As examples, the following subsections (Sections S1.5.1–S1.5.3) repeat the same simulations as in Sections 3.2.1–3.2.3 but with enabling tracking of model time by adopting 8 or 16 classes of $CaCO_3$ particles whose properties are tabulated in Tables S1 and S2. Except for the doubled numbers of simulated $CaCO_3$ classes (Tables S1 and S2), the experimental conditions are the same as those presented in Section 3.2.

S1.5.1. Bioturbation

The experiments to examine distortions of proxy signals by bioturbation in Section 3.2.1 are repeated in this section with additionally tracking model time (Fig. S10d) by simulating 8 classes of $CaCO_3$ particles in Table S1.

Before describing the results, the details on the calculation of the rain fluxes for individual $CaCO_3$ classes are presented first. When one considers a given proxy or characteristic, $CaCO_3$ classes can be grouped into 2 sets of classes, which have either the maximum or minimum value for the cosidered proxy/characteristic (Table S1). The rain fractions for the two sets can be calculated from the input value for the proxy/characteristic (e.g., Fig. S10b when considering

δ^{13}C). For instance, if the two sets of $CaCO_3$ classes have the values of A and B and the input value is given as X (cf. Fig. 3b), then the rain fractions for the two sets of classes (denoted as a and b, respectively) can be calculated as a solution of two equations: $aA + bB = X$ and $a + b = 1$. After repeating the assignment of the rain fractions for two sets of classes for all the considered proxies/characteristics (Figs. S10a–d), the rain fraction of a given class can be calculated as the product of the rain fractions for the sets that have the same properties as those of the considered class (Fig. S10e). As an example, rain fraction of class #1 (dotted black curve in Fig. S10e) is calculated as the product of the rain fractions for the sets of classes that have the maximum values for δ^{13}C, δ^{18}O and model time (solid curves in Figs. S10b–d, respectively).

The age model (the relationship between model time and diagnosed depth) is an additional output of the model by enabling time tracking (Figs. S11c and g). The age model is the same among different cases with and without bioturbation when disabling dissolution because sediment accumulates at the same rate below the mixed layer (Fig. S11c). Thus, with dissolution disabled, depth-dependent proxy signal changes can be directly converted to temporal changes with a single age model (compare Figs. S11a and b with Figs. S12a and b).

On the other hand, a single age model cannot be applied to reveal temporal changes of proxy signals when carbonate dissolution is mechanistically linked to styles of bio-mixing (Figs. S11g and h). Apparent signal shifts in depth caused by changes in the extent of dissolution or sediment accumulation rate (Figs. S11e and f) are absent when plotted against mode time using individual age models (Figs. S12d and e). It also becomes clearer that proxy signals are more effectively lost along with $CaCO_3$ particles when mixing is relatively ineffective. For example, a slight reduction of δ^{18}O peak by enabling dissolution is recognized for the no bioturbation case (see a slightly smaller peak of pink curve in Fig. S12e than in Fig. S12b).

S1.5.2. Dissolution of carbonates

The same dissolution experiments as in Section 3.2.2 (Fig. 12) are repeated in this section except with enabling model-time tracking. Instead of 4 we adopt 8 classes (Table S1) to track model time in addition to δ^{13}C and δ^{18}O. The temporal changes of the rain fractions for the 8 $CaCO_3$ classes are presented in Fig. S13b, calculated in a way described in Section S1.5.1 (Table S1 and Fig. S13b).

Perfect age models for different cases with and without bioturbation are available with enabling time tracking, with which signal change events recorded in the sediment (i.e., Fig. 13) can be plotted against model time (Fig. S14). Signal plots against model time reveal that long-term input signals are reconstructed reasonably well when dissolution is not so severe (as in experiment #1, Figs. S14a–f). However, when signals are lost by intense dissolution as in experiment #2, signal change events are significantly obscured (Figs. S14g–i). Preservation of proxy signals is better with efficient bioturbation (e.g., non-local homogeneous mixing; yellow curves in Figs. S14g and h) because bio-mixing can transfer $CaCO_3$ particles with preserved signals to locations where proxy signals are lost by dissolution along with $CaCO_3$ particles.

S1.5.3. Species-specific mixing/dissolution

Differences in recorded proxy signals in two distinctive $CaCO_3$ species with different grain sizes ('coarse' vs. 'fine' speces) are examined by simulating 8 classes of $CaCO_3$ particles in Section 3.2.3. Here we repeat the same experiments but with additionally tracking model time by simulating 16 classes of $CaCO_3$ particles in Table S2 (Fig. S15).

Using the tracked time against diagnosed depth (i.e., age model) proxy signals in the two distinctive $CaCO_3$ species can be plotted against model time (Fig. S16). As described in Section 3.2.3, apparent offsets of excursions of proxy signals and species abundance between the two species disappear (compare Figs. S16 and 15) but the reduction of the magnitude of imposed species abundance changes is still recognized especially in cases with bioturbation (Fig. S16c).

S2. Supplementary experiments

S2.1. Lysocline experiments with $V_{\mathrm{OM}} = 0$

The lysocline experiments in Section 3.1 are designed in essentially the same way as in Archer (1991). However, our results showed that $CaCO_3$ burial is enhanced compared to the estimates by Archer (1991) under sediment conditions where OM is preserved with high OM rains allowing the oxic-only OM degradation. The difference is likely caused because IMP simulates spatially and temporatly resolved diagenesis for all solid/aqueous phases including OM while $CaCO_3$ burial calculation by Archer (1991) does not account for the volume of preserved OM and the resulting burial enhancement. To reproduce the results of Archer (1991) more precisely, here we conduct the same lysocline experiments as in Section 3.1 but with assuming zero molar volume for organic matter ($V_{\mathrm{OM}} = 0$) to disable any burial enhancement by the preservation of OM.

Figs. S17 and S18 show the lysoclines with the oxic-only and oxic-anoxic OM degradation models, respectively, with $V_{\mathrm{OM}} = 0$. The assumption of $V_{\mathrm{OM}} = 0$ causes significant differences only under high OM rains with assuming the oxic-only model (compare Figs. 8 and S17) because otherwise OM is scarcely preserved. The results with the oxic-only model are now closer to the results by Archer (1991), further supporting the capability of IMP as a diagenesis simulator.

References

Aloisi, G., Wallmann, K., Haese, R. R., and Salière, J. F. (2004). Chemical, biological and hydrological controls on the ^{14}C content of cold seep carbonate crust: numerical modeling and implications for convection at cold seeps. *Chemical Geology*, 213:359–383.

Archer, D. (1991). Modeling the calcite lysocline. *Journal of Geophysical Research: Oceans*, 96(C9):17037–17050.

Barker, S., Broecker, W., Clark, E., and Hajdas, I. (2007). Radiocarbon age offsets of foraminifera resulting from differential dissolution and fragmentation within the sedimentary bioturbated zone. *Paleoceanography*, 22(2).

Broecker, W. S., Klas, M., Clark, E., Bonani, G., Ivy, S., and Wolfli, W. (1991). The influence of $CaCO_3$ dissolution on core top radiocarbon ages for deep-sea sediments. *Paleoceanography*, 6(5):593–608.

DePaolo, D. J. (2011). Surface kinetic model for isotopic and trace element fractionation during precipitation of calcite from aqueous solutions. *Geochimica et Cosmochimica Acta*, 75:1039–1056.

Hoffman, K. A. and Chiang, S. T. (2000). Computational Fluid Dynamics, vol. 1. *Engineering Education System.*

Humphreys, M. P., Gregor, L., Pierrot, D., van Heuven, S. M. A. C., Lewis, E. R., and Wallace, D. W. R. (2020). PyCO2SYS: marine carbonate system calculations in Python. *Zenodo.*

Keir, R. S. (1984). Recent increase in Pacific $CaCO_3$ dissolution: A mechanism for generating old ^{14}C ages. *Marine Geology*, 59(1-4):227–250.

Lewis, E. and Wallace, D. W. R. (1998). Program Developed for CO_2 System Calculations. *ORNL/CDIAC-105.*

Orr, J. C. and Epitalon, J. M. (2015). Improved routines to model the ocean carbonate system: mocsy 2.0. *Geoscientific Model Development*, 8:485–499.

Oxburgh, R. (1998). The Holocene preservation history of equatorial Pacific sediments. *Paleoceanography*, 13(1):50–62.

van Heuven, S., Pierrot, D., Rae, J., Lewis, E., and Wallace, D. (1998). MATLAB Program Developed for CO_2 System Calculations. *ORNL/CDIAC-105b.*

Table S1: Properties of $CaCO_3$ classes in simulations in Sections S1.5.1 and S1.5.2.

Property [a]	$CaCO_3$ class #							
	1	2	3	4	5	6	7	8
$\delta^{13}C$	+	+	−	−	+	+	−	−
$\delta^{18}O$	+	−	+	−	+	−	+	−
Time	+	+	+	+	−	−	−	−

[a] '+' and '−' denote the maximum and minimum values for $CaCO_3$ property. As an example, when $\delta^{18}O$ is tracked and its input values are between −1 and 1 ‰ for a given simulation, $CaCO_3$ classes with '−' and '+' for $\delta^{18}O$ have −1 and 1 ‰ of $\delta^{18}O$, respectively.

Table S2: Properties of $CaCO_3$ classes in simulations in Section S1.5.3.

Property [a]	$CaCO_3$ class #															
	1	2	3	4	5	6	7	8	9	10	11	12	13	14	15	16
$\delta^{13}C$	+	+	−	−	+	+	−	−	+	+	−	−	+	+	−	−
$\delta^{18}O$	+	−	+	−	+	−	+	−	+	−	+	−	+	−	+	−
Size	F	F	F	F	C	C	C	C	F	F	F	F	C	C	C	C
Time	+	+	+	+	+	+	+	+	−	−	−	−	−	−	−	−

[a] '+' and '−' denote the maximum and minimum values for $CaCO_3$ property. As an example, when $\delta^{18}O$ is tracked and its input values are between −1 and 1 ‰ for a given simulation, $CaCO_3$ classes with '−' and '+' for $\delta^{18}O$ have −1 and 1 ‰ of $\delta^{18}O$, respectively. 'F' and 'C' denote that the grain size of a $CaCO_3$ classe is 'fine' and 'coarse', respectively. 'Coarse' classes have the standard mixing and dissolution properties while classes of 'fine' size are mixed to a deeper depth (20 cm) and dissolved faster (with 10 times the standard rate constant).

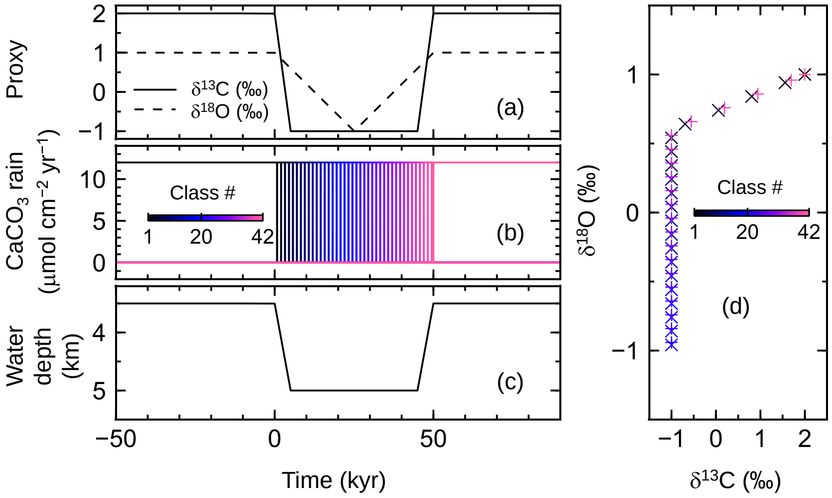

Figure S1: Timelines of proxy inputs (a), rain fluxes of individual classes of $CaCO_3$ particles (b) with different proxy values (d) and water depth changes (c) in simulations illustrating the option to adopt the time-stepping method. Except for the number of $CaCO_3$ classes and assignment of proxy and flux values to individual classes (b and d), the simulation conditions are the same as those in dissolution experiment #2 in Fig. 12.

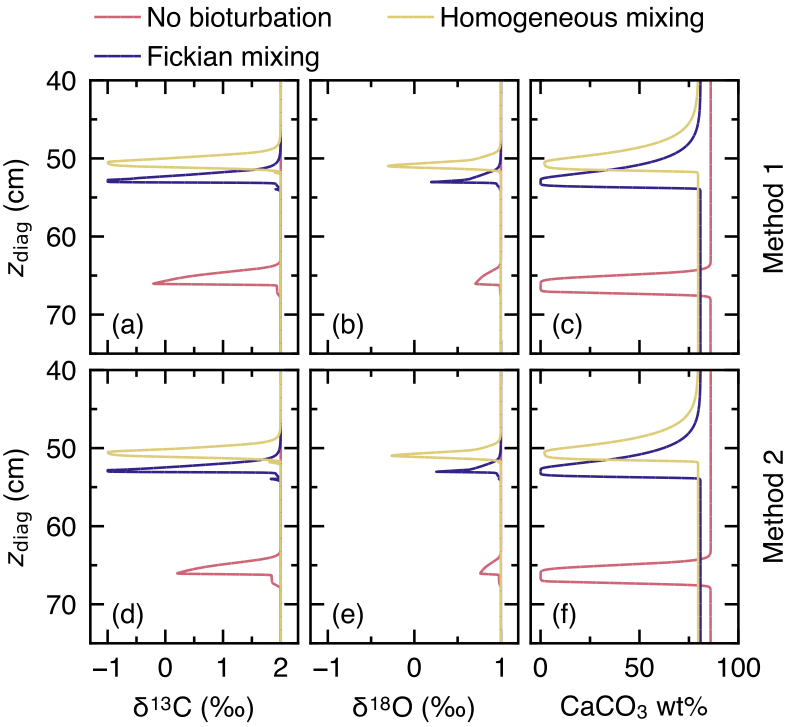

Figure S2: Proxy signals (a, b, d and e) and weight fraction of bulk $CaCO_3$ in solid sediment (c and f) in dissolution experiment #2 in Fig. 12, tracked by the time-stepping method (method 1) with 42 classes of $CaCO_3$ particles (a–c) and by the interpolating method (method 2) with 4 classes of $CaCO_3$ particles (d–f).

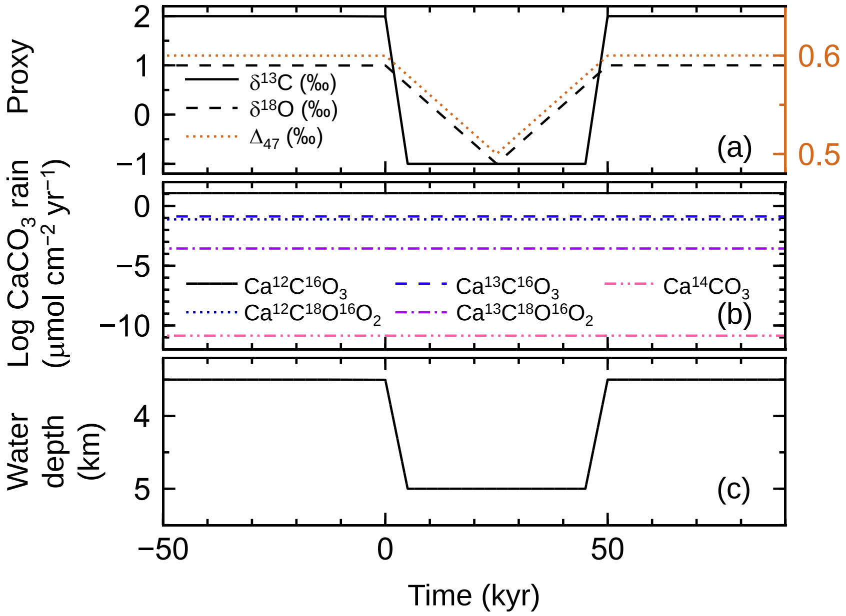

Figure S3: Timelines of proxy inputs (a), rain fluxes of individual $CaCO_3$ isotopologues (b) and water depth changes (c) in simulations illustrating the option of direct tracking of $CaCO_3$ isotopologues. In a, δ^{13}C and δ^{18}O are plotted against left vertical axis while Δ_{47} is plotted against right vertical axis. The total rain flux of $CaCO_3$ and time changes of δ^{13}C, δ^{18}O and water depth are the same as those in dissolution experiment #2 in Fig. 12. Note that in b time changes in rain fluxes of individual $CaCO_3$ isotopologues are too small to be discerned on the logarithmic scale.

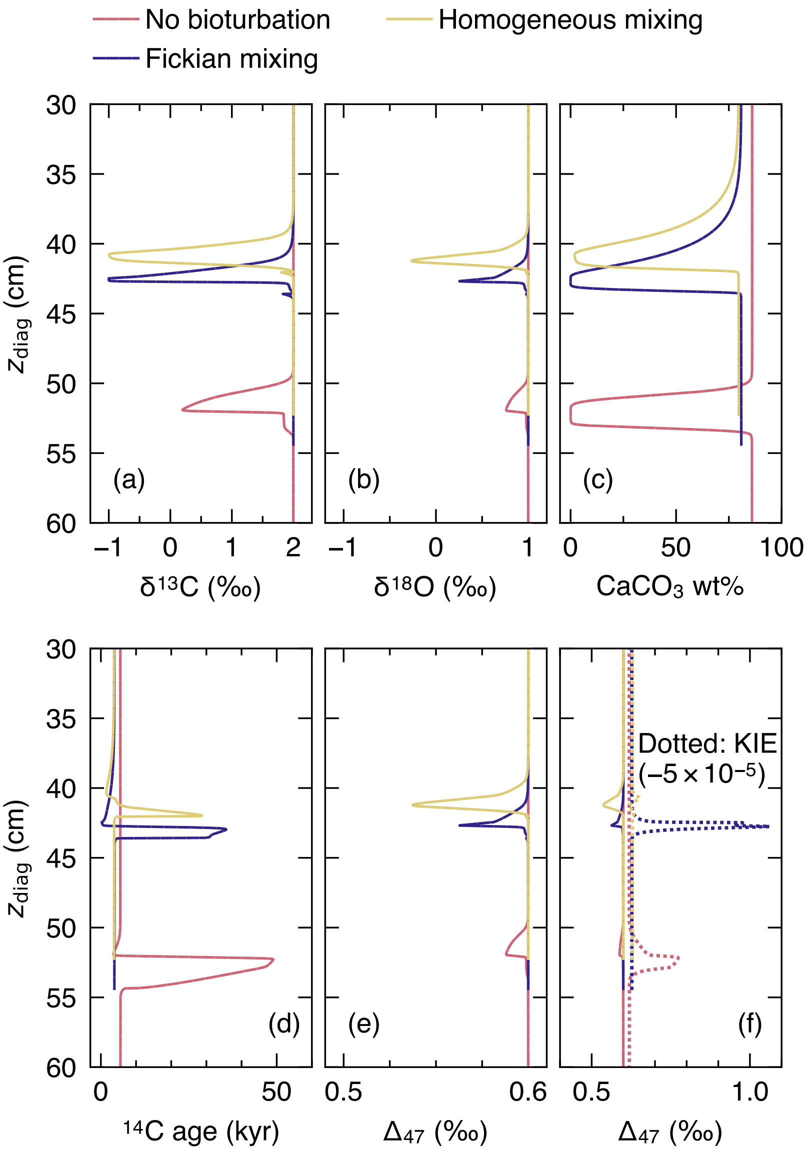

Figure S4: Proxy signals (a, b, d, e and f) and weight fraction of bulk $CaCO_3$ in solid sediment (c) tracked by 5 $CaCO_3$ isotopologues in simulations illustrating the option to directly track $CaCO_3$ isotopologues. In f, Δ_{47} distortion caused by diagenesis including a hypothetical kinetic isotope effect (KIE) of −0.005% for $Ca^{13}C^{18}O^{16}O_2$ dissolution is depicted by dotted curves.

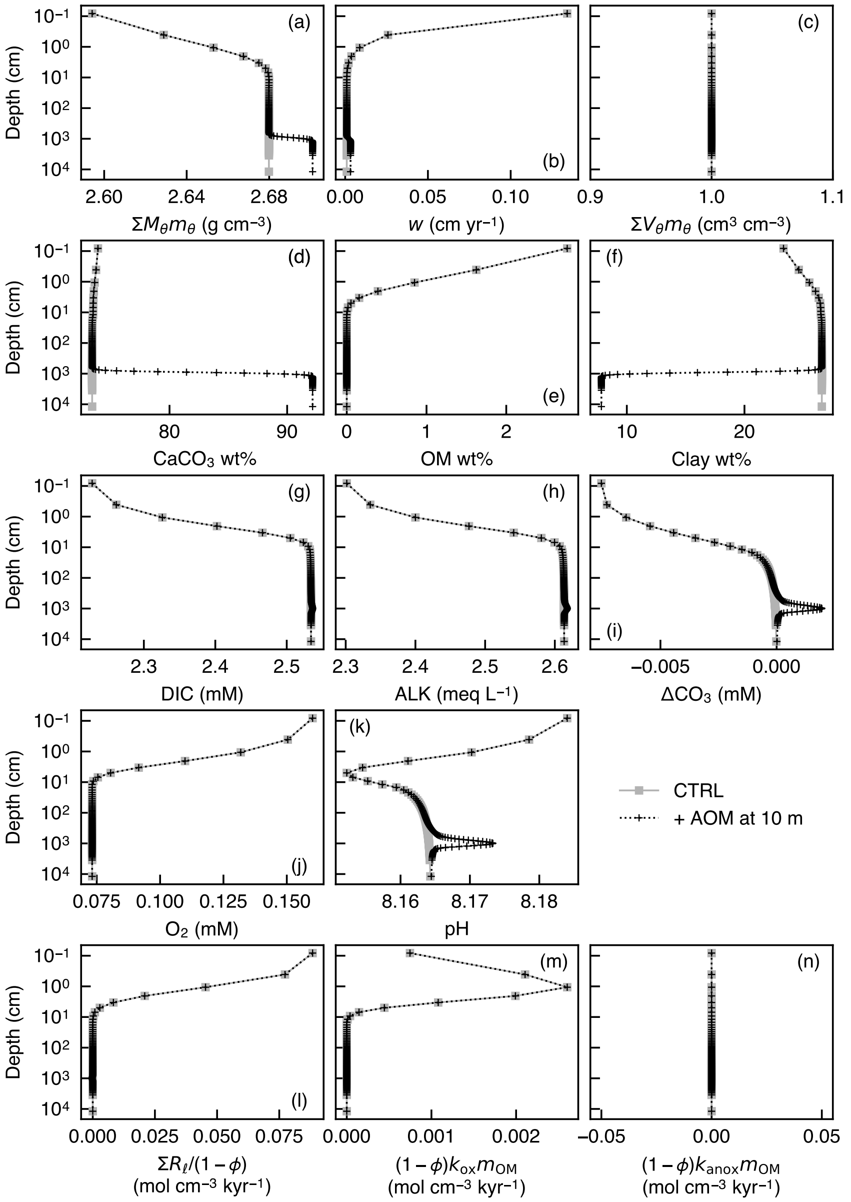

Figure S5: Effects of addition of anoxic oxidation of methane (AOM) on $CaCO_3$ diagenesis. Shown are: steady-state depth profiles of density (a) and volume fraction (c) of solid sediment, burial velocity (b), weight fractions of bulk $CaCO_3$ (d), organic matter (e) and non-reactive detrital materials (f) in solid sediment, porewater concentrations of total dissolved CO_2 species (g), carbonate alkalinity (h) and oxygen (j), deviation of porewater carbonate concentration from that in equilibrium with $CaCO_3$ (i), porewater pH (k), dissolution rate of $CaCO_3$ (l) and decomposition rate of organic matter in the oxic (m) and anoxic (n) zone of sediment. The calculations assume 4 classes of $CaCO_3$ particles and Fickian mixing for bioturbation. Precipitation of $CaCO_3$ is allowed. The control experiment ('CTRL', grey curves) assumes the default boundary conditions in Table 1 except for the water depth (4 km) and total sediment depth (z_{tot} = 20000 cm). The AOM simulating experiment ('+AOM at 10 m', black curves) adds DIC and ALK fluxes (12 and 24 µmol cm^{-2} yr^{-1}, respectively) at 10 m to the boundary conditions of the control experiment. See Section S1.2 for further details on the experimental conditions.

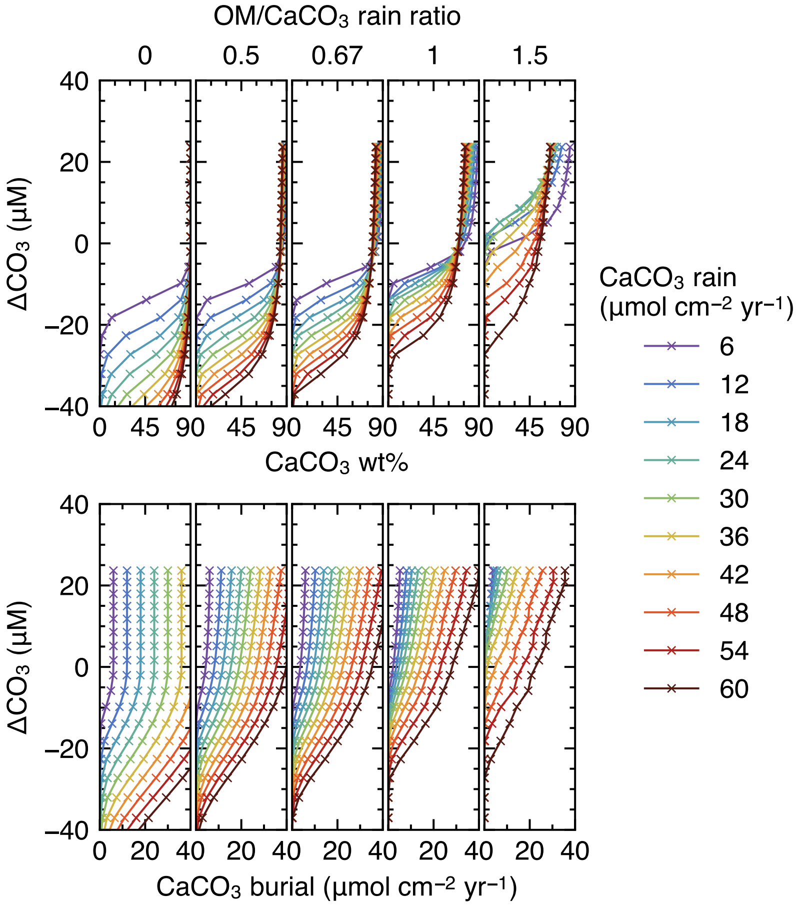

Figure S6: Estimated $CaCO_3$ weight fractions in mixed layer and burial fluxes as functions of $CaCO_3$ saturation degree (ΔCO_3) and rain fluxes, with enabling only oxic degradation of organic matter. The results shown are from the model which adopts a shallower sediment depth (50 cm), single class of $CaCO_3$ particles, Fickian mixing for bioturbation and mocsy 2.0 to calculate CO_2 chemistry.

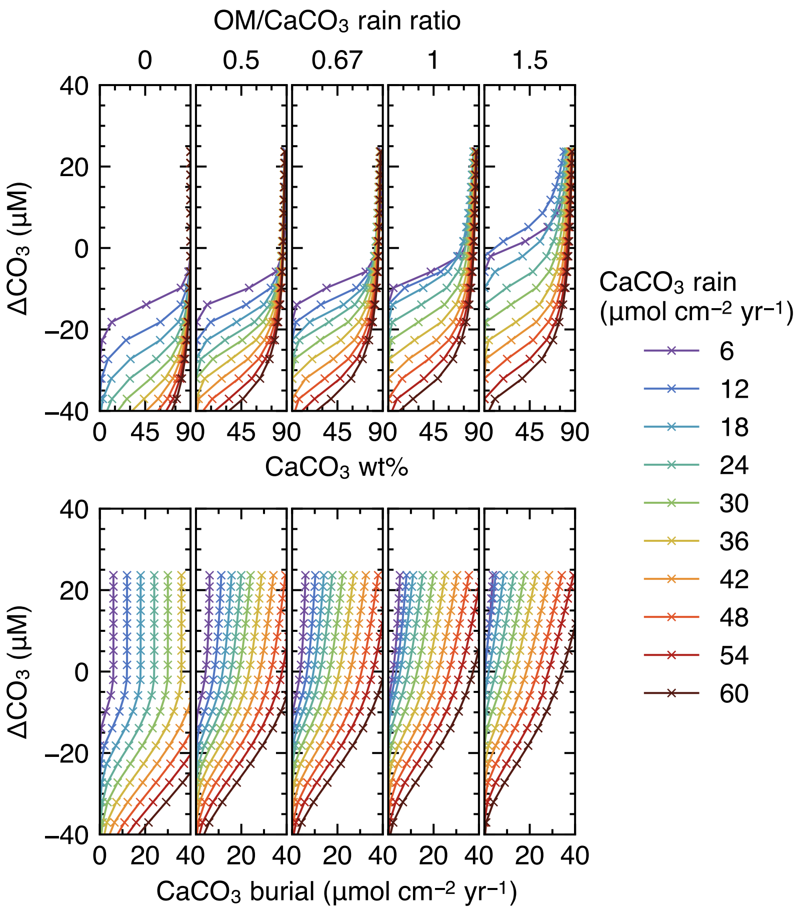

Figure S7: As for Fig. S6 except enabling both oxic and anoxic degradation of organic matter.

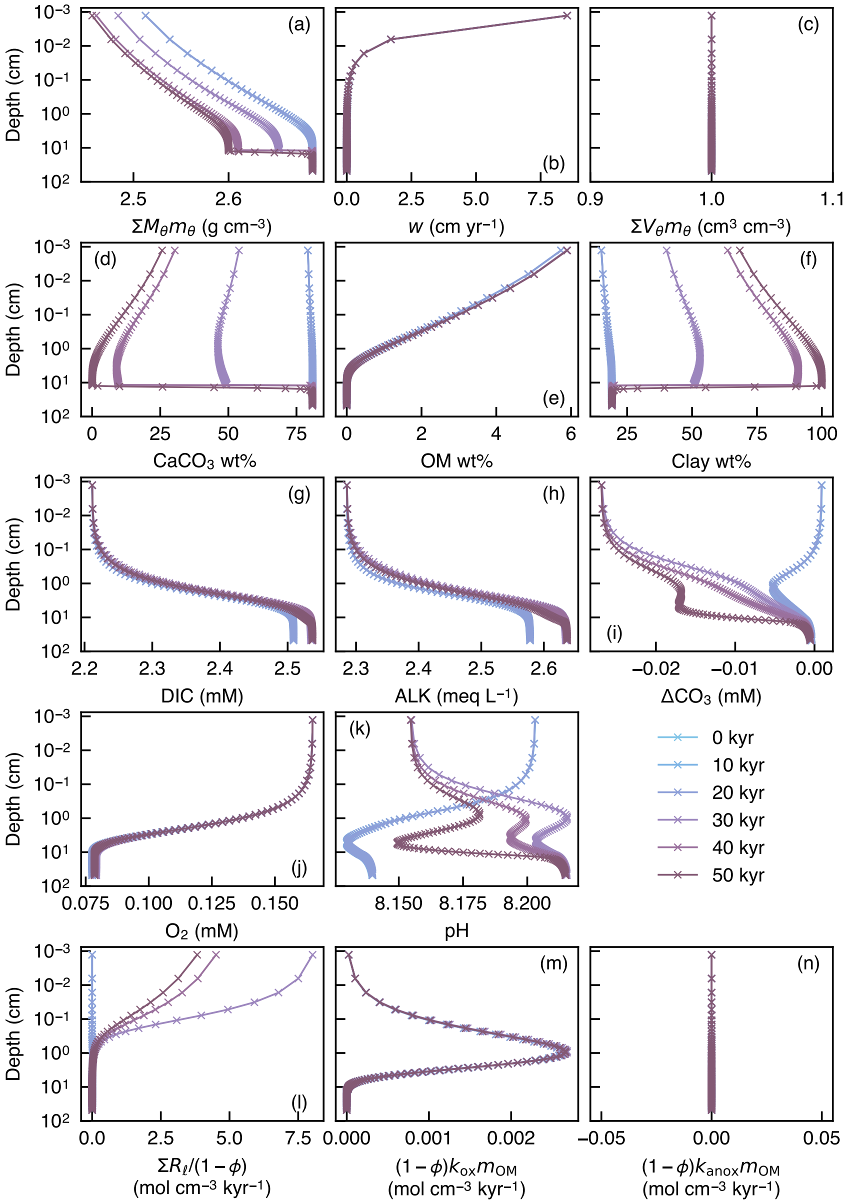

Figure S8: Depth profiles of density (a) and volume fraction (c) of solid sediment, burial velocity (b), weight fractions of bulk CaCO$_3$ (d), organic matter (e) and non-reactive detrital materials (f) in solid sediment, porewater concentrations of total dissolved CO$_2$ species (g), carbonate alkalinity (h) and oxygen (j), deviation of porewater carbonate concentration from that in equilibrium with CaCO$_3$ (i), porewater pH (k), dissolution rate of CaCO$_3$ (l) and decomposition rate of organic matter in the oxic (m) and anoxic (n) zone of sediment, as a function of time. The experimental conditions are the same as those for Fig. 7 except in a shallower ($z_{\mathrm{tot}} = 50$ cm) and less irregular ($\beta = 1.05$) sediment grid.

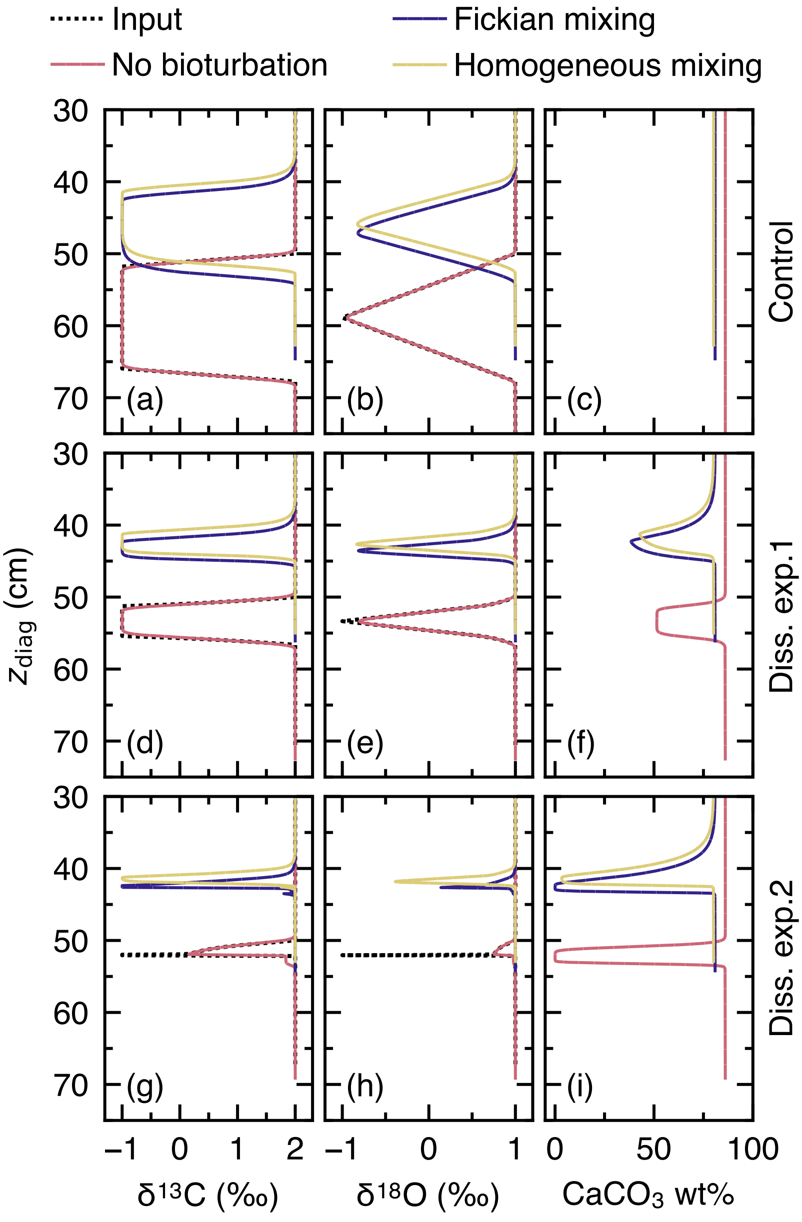

Figure S9: Proxy signals (a, b, d, e, g and h) and weight fraction of bulk $\mathrm{CaCO_3}$ in solid sediment (c, f and i) in the same dissolution experiments as in Fig. 13 except in a shallower ($z_{\rm tot}$ = 50 cm) and less irregular (β = 1.05) sediment grid.

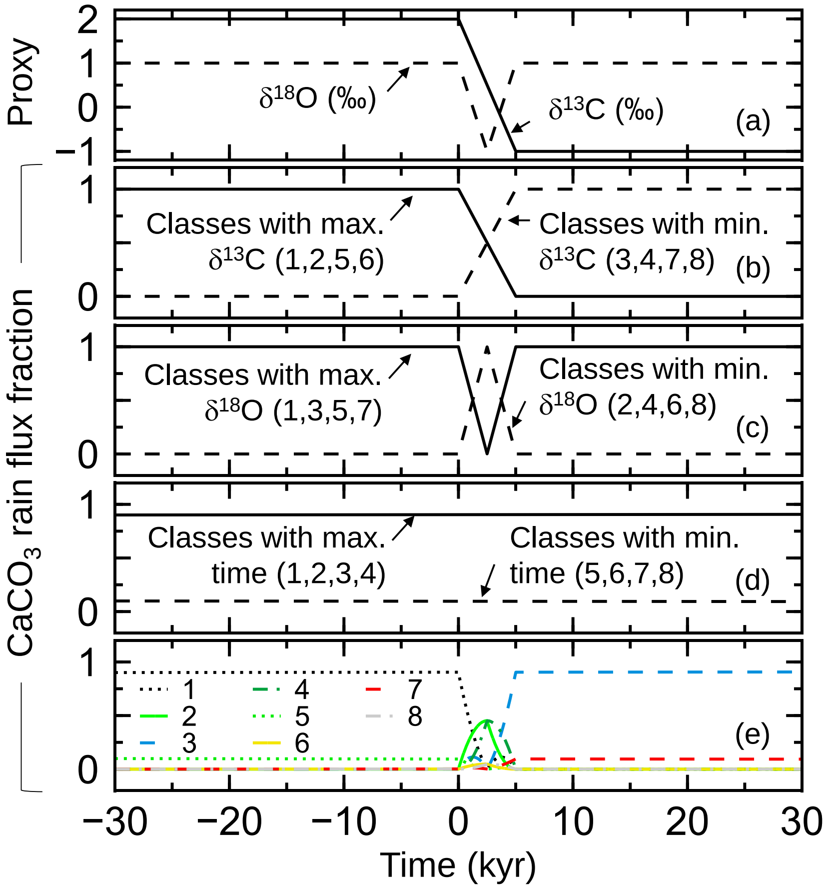

Figure S10: Timelines of proxy inputs (a) and rain fractions for pairs of CaCO$_3$ classes that have the maximum and minimum proxy values (b and c) and model time (d), and for individual CaCO$_3$ classes (e), in simulations examining signal distortion by bioturbation. See Table S1 for the properties of individual CaCO$_3$ classes.

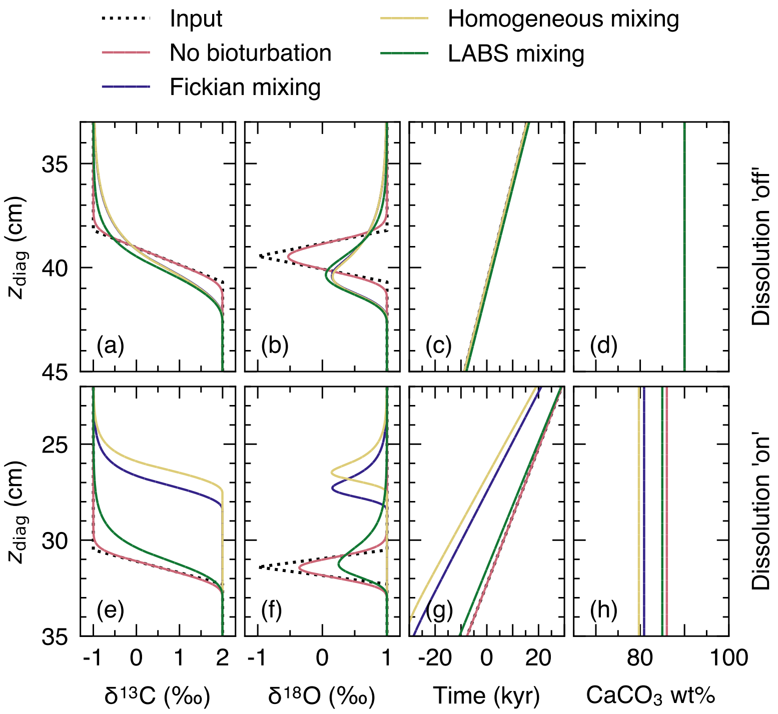

Figure S11: Proxy signals (a, b, e and f), model time (c and g) and weight fraction of bulk $CaCO_3$ in solid sediment (d and h) tracked by 8 classes of $CaCO_3$ particles plotted against diagnosed depth in simulations examining signal distortion by bioturbation. In a–d, dissolution rate constants of all $CaCO_3$ classes are fixed at zero, while in e–h, at the default value (Table 1).

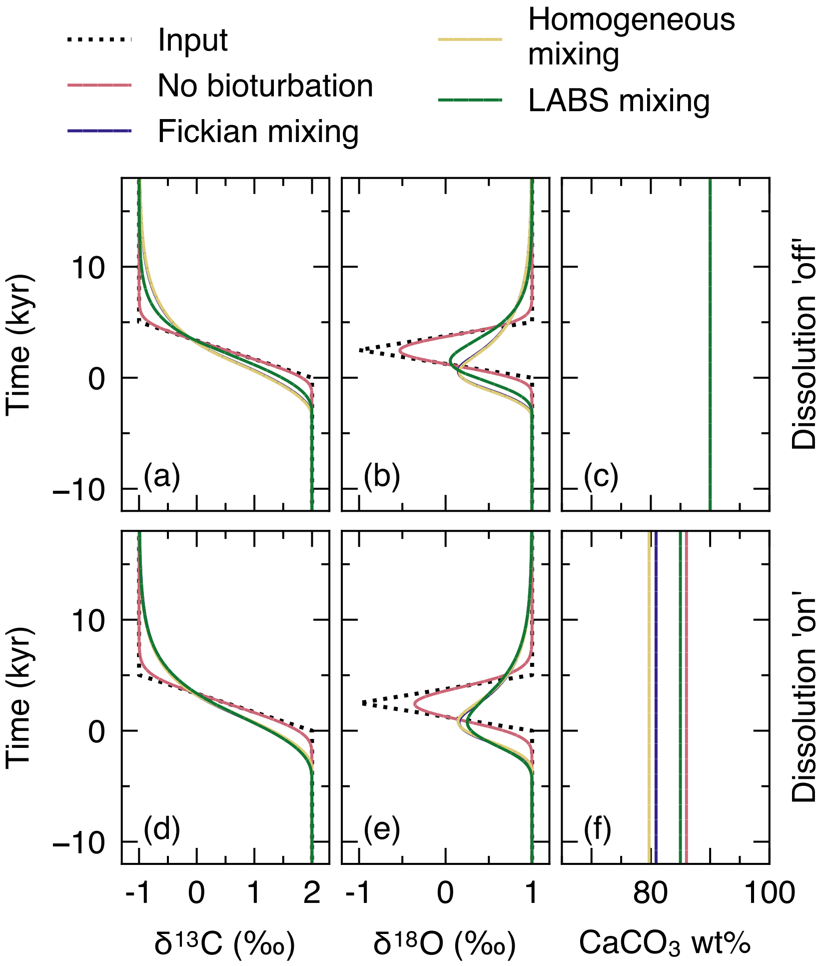

Figure S12: Proxy signals (a, b, d and e) and weight fraction of bulk $CaCO_3$ in solid sediment (c and f) plotted against model time in simulations examining signal distortion by bioturbation. In a–c, dissolution rate constants of all $CaCO_3$ classes are fixed at zero, while in d–f, at the default value (Table 1).

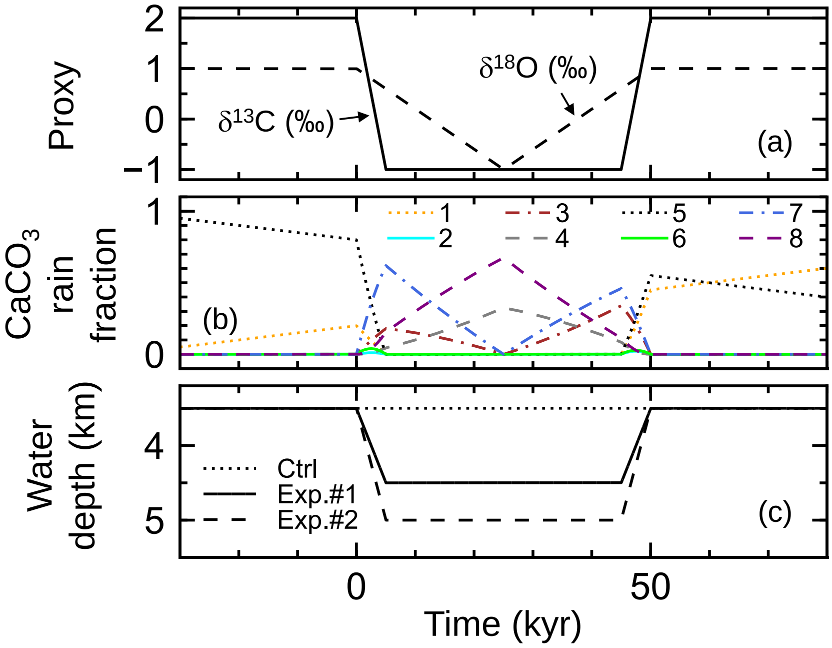

Figure S13: Timelines of proxy inputs (a), rain fractions of individual classes of $CaCO_3$ particles (b) and water depth changes (c) in simulations examining signal distortion by $CaCO_3$ dissolution. Two different water depth changes are considered, denoted as dissolution experiments #1 and 2 (c). One set of experiments was conducted without changing the water depth for comparison (dotted line in c). See Table S1 for the properties of individual $CaCO_3$ classes.

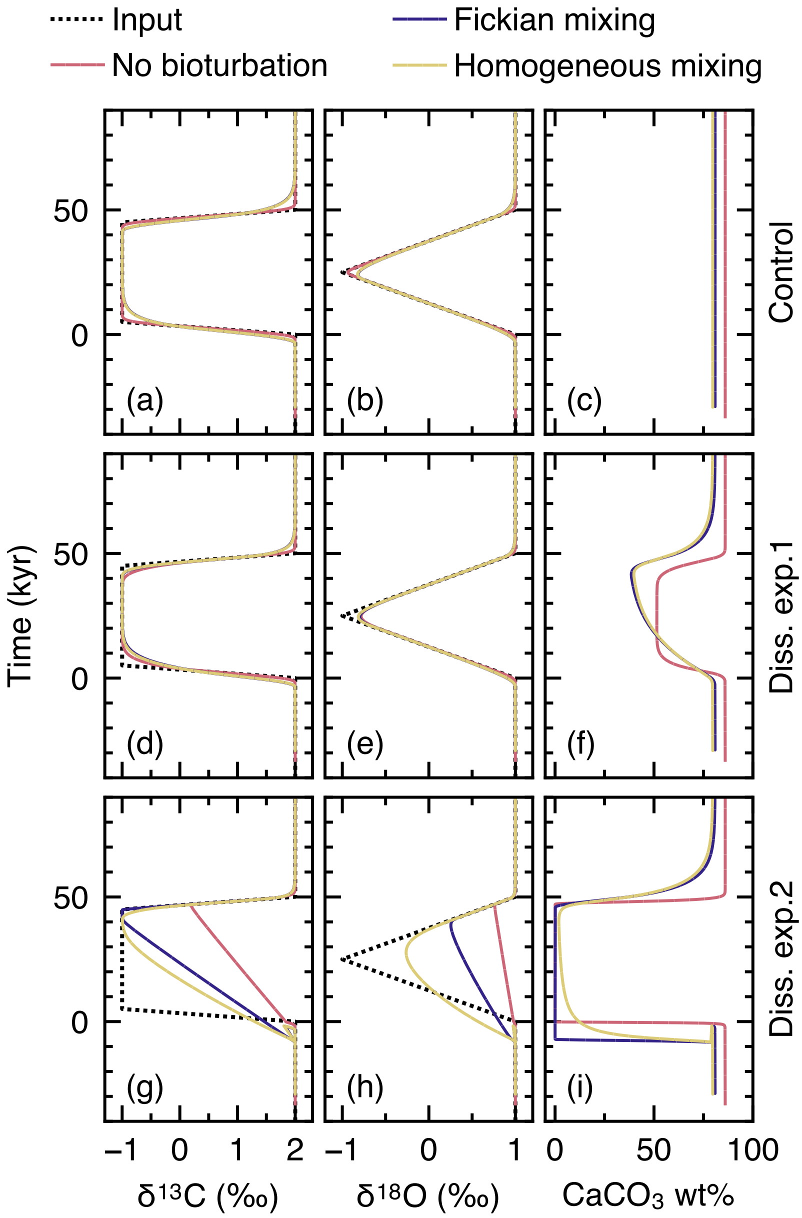

Figure S14: Proxy signals (a, b, d, e, g and h) and weight fraction of bulk $CaCO_3$ in solid sediment (c, f and i) tracked by 8 classes of $CaCO_3$ particles plotted against model time in simulations examining signal distortion by $CaCO_3$ dissolution. Two different water depth changes are considered, denoted as dissolution experiments #1 and 2, and compared to the case without water depth change, denoted as control. See Fig. S13c for the assumed water depth changes.

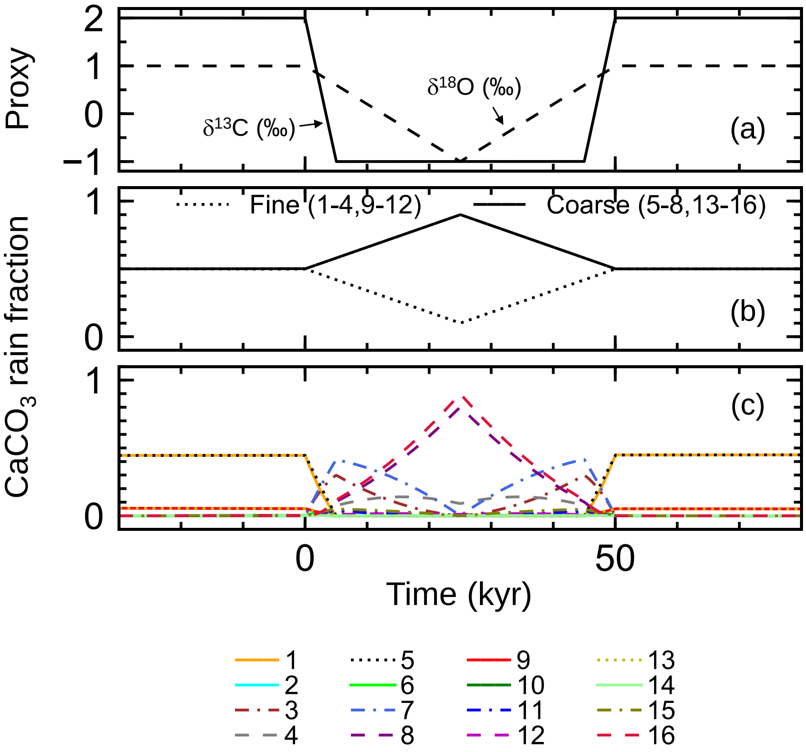

Figure S15: Timelines of proxy inputs (a) and rain fractions of fine and coarse $CaCO_3$ species (b) and individual classes of $CaCO_3$ particles (c) in simulations examining effect of species-specific mixing/dissolution properties. See the legend located at the bottom of diagram for the correspondence between $CaCO_3$ classes and types of curve in c. See Table S2 for the properties of individual $CaCO_3$ classes.

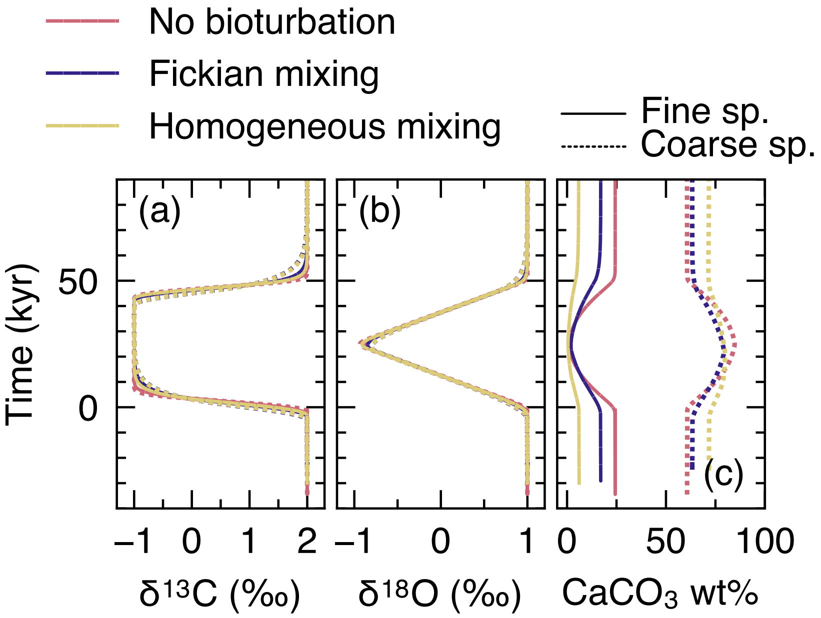

Figure S16: Proxy signals (a and b) and weight fraction of bulk $CaCO_3$ in solid sediment (c) for fine and coarse $CaCO_3$ species (solid and dotted curves, respectively) tracked by 16 classes of $CaCO_3$ particles plotted against model time in simulations examining effect of species-specific mixing/dissolution properties.

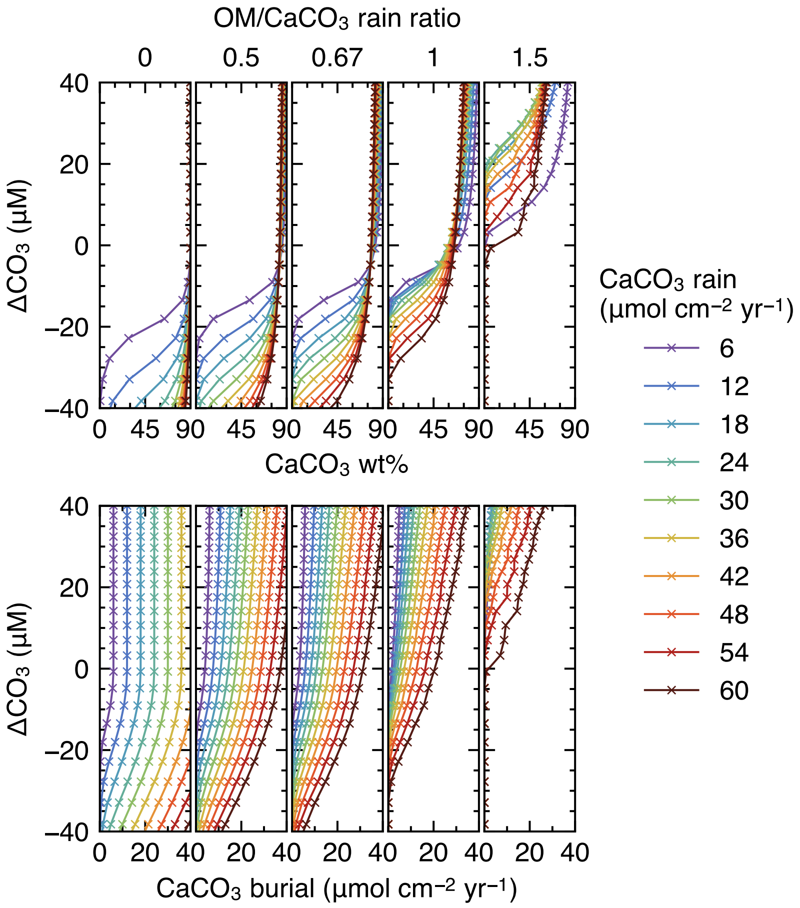

Figure S17: As for Fig. S6 except adopting the simplified scheme in Tables 2 and 3 to calculate porewater CO_2 chemistry instead of mocsy 2.0 and assuming zero volume for OM ($V_{\mathrm{OM}} = 0$).

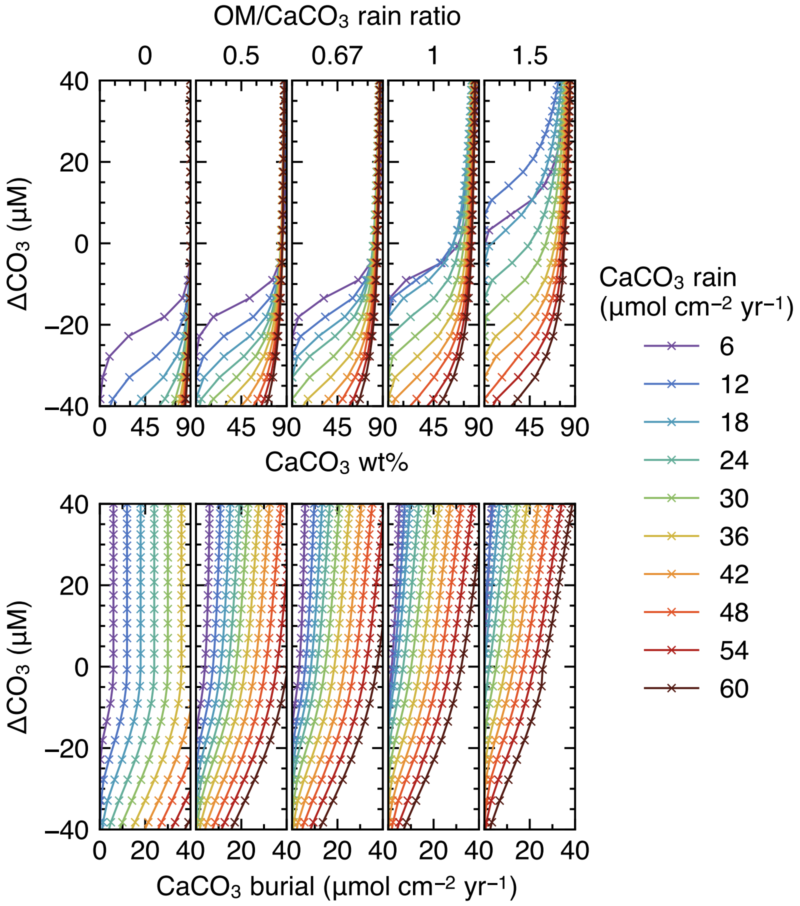

Figure S18: As for Fig. S17, except enabling both oxic and anoxic degradation of organic matter.